

Low interface reflection of rod-type photonic crystals: a bottom up approach

C. Martijn de Sterke^a, T.P. White^a, L.C. Botten^b, and R.C. McPhedran^a

^a School of Physics and Centre for Ultrahigh-bandwidth Devices for Optical Systems (CUDOS), University of Sydney, NSW 2006, Australia;

^b Department of Mathematical Sciences and Centre for Ultrahigh-bandwidth Devices for Optical Systems (CUDOS), University of Technology, Sydney, NSW 2007, Australia.

ABSTRACT

We consider coupling between free-space and rod-type photonic crystals using semi-analytic 2D methods, and find that for frequencies in the second and third bands this coupling is almost perfect over a large range of angles. We explain this remarkable property in terms of the scattering resonances of the individual inclusions and then confirm the presence of this effect in fully 3D FDTD calculations.

Keywords: Photonic crystals

1. INTRODUCTION

Many of the key applications of photonic crystals (PCs) depend on their ability to tailor the propagation of light at frequencies in a band. Examples are autocollimation, in which the light propagates with very small diffraction, and the superprism, in which the direction of light propagation depends strongly on the incident angle or on the wavelength of the light. However, in all applications of this type the light needs to be coupled into and out of the PC and it is important that this be accomplished efficiently. Otherwise, not only does the optical power decrease, but also the stray light may affect the device operation.

The coupling of light between free space and air-hole type photonic crystals has been studied previously by different groups. They found the coupling efficiency to be generally insufficient and devised different interface modifications to improve the coupling. These modifications either involve changing the size or shape of the air holes,^{1,2} or adding an additional row of holes, which acts as an anti-reflection coating.³ In contrast, here we investigate the transmission into a rod-type photonic crystal, and show in Section 2, in a strictly two-dimensional analysis, that for some wavelengths this transmission can be close to perfect for a very wide range of incoming angles. We show in Section 5 that this property carries over to three-dimensional geometries. In the intervening sections we investigate the highly efficient coupling and demonstrate that it is associated with resonances of the individual inclusions: in Section 3 we review the properties of high-index cylinders in a low-index background, while in Section 4 we link these, via the properties of diffraction gratings, with PCs. Our argument shows that the high-coupling efficiency only occurs in rod-type PC, and not in PCs of the air hole-type.

2. PLANE WAVE REFLECTION AND TRANSMISSION PROPERTIES

We begin with the 2D structure Fig. 1, in which a plane wave is incident at an angle ϕ_0 onto a semi-infinite 2D PC. The reflection of the incident field is characterized by the matrix R_∞ , defined as the reflection scattering matrix for a plane wave incident from free-space onto a semi-infinite PC. In this notation, the $(pq)^{\text{th}}$ element of R_∞ is the complex amplitude for reflection into grating order p for a plane wave incident in order q with unit amplitude. We calculate R_∞ using a Bloch mode scattering matrix method (BMM)^{4,5} derived from the solution of a transfer matrix eigenvalue problem

$$\mathcal{T}f = \mu f \quad (1)$$

Further author information: (Send correspondence to C.M.de S.)

C.M. de S.: E-mail: m.desterke@physics.usyd.edu.au, Telephone: 61 2 9351 2906

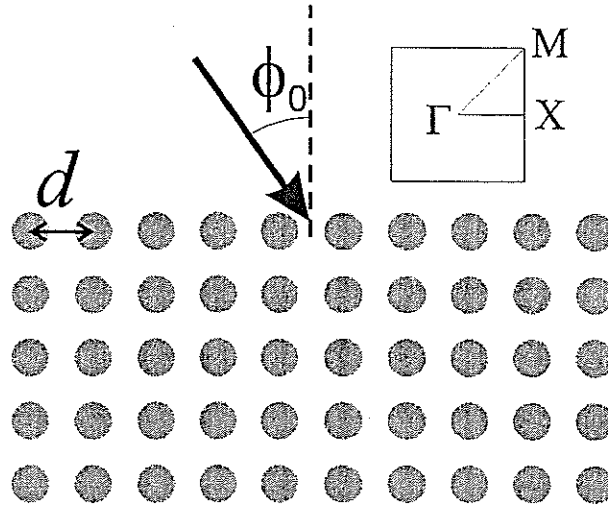


Figure 1. Geometry used to calculate the transmission of a plane wave incident on a semi-infinite PC at an angle ϕ_0 .

for the Bloch modes of the bulk structure, where \mathcal{T} is the transfer matrix for a single PC layer. The philosophy of our treatment is that we consider the PC to consist of layers, each of which constitutes a *grating*. The properties of these gratings can be calculated using standard techniques such as integral equation methods, differential methods, modal theories and multipole methods (see, for example, the work by Maystre,⁶ Neviere and Popov,⁷ or Botten *et al.*⁸). The PC properties are then determined by suitable combining the grating properties. Each of the gratings is characterized by plane wave reflection and transmission scattering matrices and we may express the transfer matrix in the form

$$\mathcal{T} = \begin{pmatrix} T - R'T'^{-1}R & R'T'^{-1} \\ -T'^{-1}R' & T'^{-1} \end{pmatrix} \quad (2)$$

where R and T denote the reflection and transmission scattering matrices for a "padded" grating layer for incidence from above, and R' and T' being the corresponding quantities for incidence from below. In Eq. (1), $f = [f_-^T \ f_+^T]^T$ denotes the Bloch mode where f_{\pm} are vector of plane wave coefficients that define the Bloch mode on a line $y = y_j$ midway between each of the grating layers according to

$$V^{(j)}(x, y) = \sum_{p=-\infty}^{\infty} \chi_p^{-1/2} \left[f_p^{(j)-} e^{-i\chi_p(y-y_j)} + f_p^{(j)+} e^{i\chi_p(y-y_j)} \right] e^{i\alpha_p x}. \quad (3)$$

Here, $\alpha_p = \alpha_0 + pK$, $\chi_p = \sqrt{k^2 - \alpha_p^2}$, $K = 2\pi/d$ and $k = 2\pi/\lambda$. Then, following the treatment by Botten *et al.*,⁴ we may write $R_{\infty} = F_+ F_-^{-1}$, where F_- and F_+ are matrices whose columns contain the forward (f^-) and backward (f^+) propagating parts of the plane wave representations of the Bloch modes of the bulk structure.

Since we are interested in the reflected power, and no energy is carried away from the PC interface by the evanescent states, R_{∞} is truncated to contain only those elements corresponding to propagating plane wave orders. Thus, when only a single reflected order is supported, R_{∞} can be treated as a scalar and the total reflected power is $\varepsilon_R = |(R_{\infty})_{00}|^2$. When multiple reflected orders are present, the total reflectance is calculated as a sum over the reflectance into each order. For the purely 2D structures composed of lossless dielectrics considered here, there are no additional loss mechanisms and so the transmitted power is simply $\varepsilon_T = 1 - \varepsilon_R$.

As we shall see, the BMM is a powerful tool for understanding single interface properties as it allows semi-infinite structures to be studied without the need for absorbing boundary conditions, allowing the effect of interface reflection to be isolated from the coherent reflection effects observed in structures with a finite number of PC layers. The BMM also provides a rigorous mathematical framework for studying how each component of the PC contributes to the properties of the bulk structure. As already mentioned, in our treatment, the bulk PC properties are calculated from the scattering properties of the individual grating layers which, in turn, are derived

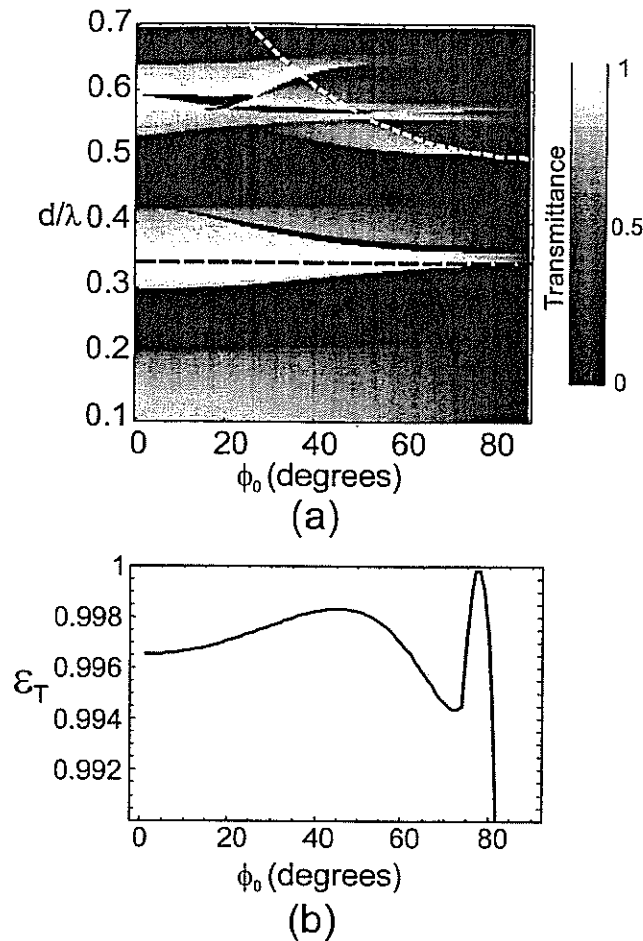


Figure 2. (a) Transmittance ε_T versus dimensionless frequency d/λ and incident angle ϕ_0 for the 2D PC described in the text. The dashed white curve indicates the maximum frequency for which a single diffracted grating order condition exists (see Section 3). (b) Transmittance versus ϕ_0 at $d/\lambda = 0.34$, indicated by the dashed black line in (a).

using a multipole method that implicitly includes the scattering characteristics of the individual cylinders. This systematic breakdown of the structure into basic components is used in Sections 4.1 and 4.2 to explain the origin of the highly efficient transmission illustrated in Figure 2.

Figure 2(a) shows the transmittance of an TM polarized incident plane wave (i.e., with the electric field parallel to the cylinders) as a function of the angle of incidence ϕ_0 and normalized frequency d/λ for a square lattice PC of rods with $\nu_c = 3.0$ and $r_c = 0.34d$. Note the white high transmission “finger” crossing the diagram at a dimensionless frequency of $d/\lambda \approx 0.34$ lying in the second band. At this frequency, indicated by the black dashed line in Fig. 2(a), the transmittance into the PC exceeds 99.4% for incident angles $0^\circ \leq \phi_0 \lesssim 80^\circ$, as shown in Fig. 2(b). A high transmission region ($\varepsilon_T > 99.5\%$) also exists in the third band near $d/\lambda = 0.58$, although this only extends to incident angles of about 30° . In contrast, the transmittance into the first band does not exceed 90%. Similar features to those shown in Fig. 2 occur in a wide range of rod-type PC structures, for both *TE* (magnetic field parallel to cylinders) and *TM* polarizations and for both square and triangular lattices. We also observe that the transmission peaks depend only weakly on the lattice period and incident angle and are almost identical for square and triangular lattices formed from the same rods. From this we are led to deduce that the near-perfect transmission features observed in Fig. 2 follow from the properties of individual rods rather than of the bulk lattice.

While in the remainder of this paper we present numerical results for the PC considered in this section,

the results are generally applicable. In following sections, we show the high-transmission properties originate from the individual scattering characteristics of the high-index rods, which influence the properties of a layer of cylinders, and in turn the properties of the 2D lattice of rods. In Section 3, we discuss the relevant scattering properties of a single dielectric cylinder: the scattering cross-section and the asymmetry parameter.

3. SINGLE CYLINDER SCATTERING

Although photonic crystals rely intrinsically on coherent scattering for many of their unique properties, the individual scattering elements contribute to the detailed characteristics of the structure. For example the correspondence between the position of bandgaps in three-dimensional (3D) PCs formed from dielectric spheres, and the Mie resonances of the spheres has been demonstrated.^{9,10} To our knowledge, however, the relationship between scattering resonances and PC transmittance has not been directly studied. Accordingly, we show here that not only is there a correspondence between cylinder resonances and band position, but also a direct relationship between forward scattering and the transmittance of plane waves incident on a PC. While the results we present in Sections 3, 4.1 and 4.2 are strictly 2D, we go on to show that the conclusions are generic and extend to 3D. Here, we consider TM polarization only, noting that qualitatively similar results are also found for TE polarization.

We begin by considering the scattering of a plane wave by a single cylinder of radius r_c and refractive index ν_c . Exterior to the cylinder the field is expanded in a cylindrical harmonic basis

$$V(r) = \sum_{n=-\infty}^{\infty} \left[a_n J_n(kr) + b_n H_n^{(1)}(kr) \right] e^{in\theta}, \quad (4)$$

where $(r, \theta) = (x, y)$, with $x = r \cos \theta$ and $y = r \sin \theta$. Note that in this geometry, the forward and backward scattering are respectively $\theta = \mp \pi/2$. The outgoing, scattered field is associated with the coefficients $b = [b_n]$ while the incident field is characterized by the coefficients $a = [a_n] = [(-1)^n]$, for an incident field $V_i = \exp(-ikr \sin \theta)$. The a and b coefficients are linked by the field continuity equations which impose the relationship^{11,12}

$$b_n = R_n a_n, \quad \text{where} \quad R_n = -\frac{1}{1 + iM_n} \quad \text{with} \quad M_n = \frac{\nu_c J'_n(k\nu_c r_c) Y_n(kr_c) - J_n(k\nu_c r_c) Y'_n(kr_c)}{\nu_c J'_n(k\nu_c r_c) J_n(kr_c) - J_n(k\nu_c r_c) J'_n(kr_c)} \quad (5)$$

for TM polarization. We may then deduce the far field form of the scattered field, based on the large argument asymptotics of the Hankel functions¹³:

$$V_s(r) \approx \sqrt{\frac{2}{\pi kr}} e^{i(kr - \pi/4)} T_c(\theta) \quad \text{where} \quad T_c(\theta) = \sum_n b_n e^{in(\theta - \pi/2)}. \quad (6)$$

Two parameters that help to characterize the scattering are the scattering cross-section per unit cylinder length

$$c_{\text{scat}} = \frac{2}{\pi k} \int_{-\pi}^{\pi} |T_c(\theta)|^2 d\theta = \frac{4}{k} \sum_{n=-\infty}^{\infty} |b_n|^2, \quad (7)$$

and the asymmetry parameter, the weighted average of $-\sin(\theta)$ with respect to the scattering intensity

$$g = -\langle \sin(\theta) \rangle = -\frac{\int_{-\pi}^{\pi} |T_c(\theta)|^2 \sin(\theta) d\theta}{\int_{-\pi}^{\pi} |T_c(\theta)|^2 d\theta}.$$

Here, $|g| < 1$, and $g > 0$ ($g < 0$) corresponds to dominant forward (backward) scattering.

Figure 3(a) shows the normal incidence transmittance spectrum for the square PC lattice considered in Figure 2. The curves in Figures 3(b) and 3(c) show the scattering cross-section and asymmetry parameter respectively versus r_c/λ for a single cylinder of radius r_c and index $\nu_c = 3.0$ in air. In both plots, the solid curve is calculated for a multipole truncation order of $N_m = 3$, where Eq. (6) is summed over $n = -N_m, -N_m + 1, \dots, N_m$. The remaining curves correspond to truncation orders of $N_m = 0, 1, 2$. Observe that the single

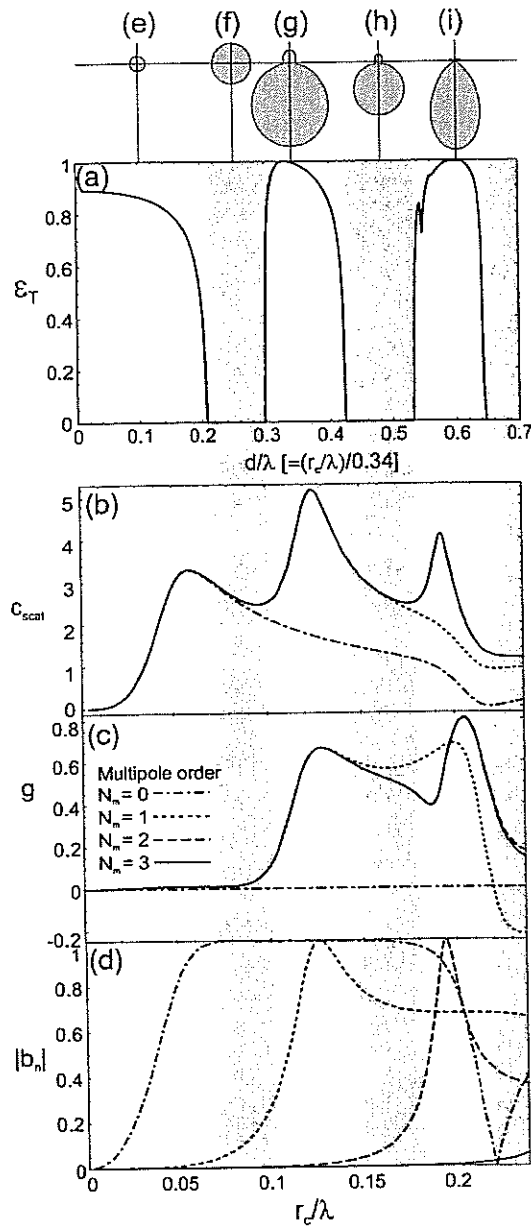


Figure 3. (a) Normal incidence transmittance for the PC lattice considered in Fig. 2. (b) and (c): Single cylinder scattering cross-section and asymmetry parameter respectively, plotted as a function of r_c/λ for the same frequency range as (a). Both parameters are calculated for multipole truncation orders $N_m = 0, 1, 2, 3$, where the $N_m = 3$ curve (solid) is converged to within graphical accuracy. (d) Multipole scattering coefficients $|b_n|$ plotted for $n = 0, 1, 2, 3$. Shaded regions in (a)–(d) indicate the band-gaps of the bulk PC. (e)–(i): Scattering patterns given by $|T(\theta)|^2/k$ for $r_c/\lambda = 0.034, 0.085, 0.116, 0.163$ and 0.204 for light incident from above.

monopole term ($N_m = 0$) describes accurately the single cylinder properties for frequencies up to the first PC band, while the dipole approximation ($N_m = 1$) is sufficient for the second band. While additional multipole terms are required in the field expansion for higher frequencies, the $N_m = 3$ curves in Fig. 3(b) and (c) have converged to graphical accuracy for the plotted frequency range. The relative importance of each multipole order can also be inferred from Fig. 3(d) which shows the amplitudes of the first four multipole coefficients $|b_n|$. In Section 4.2 we use the dipole approximation to derive a semi-analytic result relating the single cylinder scattering

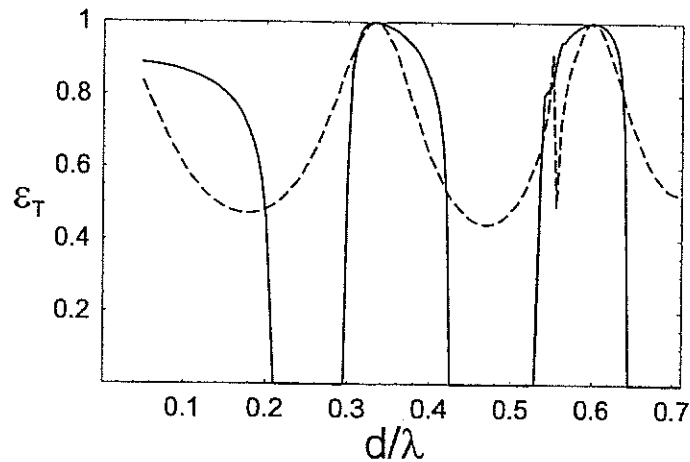


Figure 4. Normal incidence grating (dashed curve) and PC (solid curve) transmittance spectra for the PC considered in Section 2.

resonances to the transmission of a grating.

Figures 3(a) and (b) show a clear correspondence between the band position (indicated by non-zero transmittance) and peaks in c_{scat} , as observed previously.^{10,14} This does not explain, however, why the transmittance into the second and third bands exceeds 99%, whereas transmittance into the first band is less than 90%. To understand this feature, it is necessary to consider the direction of the scattered fields, as measured by the asymmetry parameter in Fig. 3(c) and the scattering patterns Figs 3(e)–(i) at various frequencies. The scattering patterns are polar plots of $|T_c(\theta)|^2/k$, such that the area enclosed by each diagram is proportional to c_{scat} . In the second and third bands, where the transmittance is highest, the peak in c_{scat} coincides approximately with a peak in g , indicating a forward scattering resonance. In the first band g remains positive but approaches zero, despite there being a small, broad peak in c_{scat} . Thus, although there is still significant scattering from each cylinder at low frequencies, the scattering is almost isotropic, with Eqs (5)–(7) being dominated by the b_0 (monopole) term as discussed above. This can also be observed in the scattering patterns in Fig. 3(e) and (f). As the frequency is increased, higher-order scattering terms become significant and can result in strong directional scattering. For example, the c_{scat} peaks near $d/\lambda = 0.36$ ($r_c/\lambda = 0.112$) and $d/\lambda = 0.60$ ($r_c/\lambda = 0.204$) correspond to maxima in b_1 and b_2 respectively, as seen in Fig. 3(d). Each of these resonances results in strong forward scattering as indicated by the g curve of Fig. 3(c) and the scattering patterns in Figs 3(g) and (i).

The results of Figs 3, while not conclusive proof that individual cylinder resonances enhance the transmittance into a PC, nevertheless provide a plausible and physically intuitive explanation for the results in Fig. 2. In what follows, we undertake a rigorous mathematical analysis to demonstrate the relationship between the transmission properties of a grating and those of a bulk PC, and, in turn, the corresponding relationships between single cylinder resonances and the grating transmission properties.

4. RIGOROUS ANALYSIS

4.1. Relationship between grating and PC transmission properties

We now build the link between the transmission properties of a the semi-infinite PC and its constituent gratings in the long wavelength regime for which only a single plane wave order is propagating in either reflection or transmission. For a PC consisting of dielectric rods in free-space, this corresponds to normalized frequencies of $d/\lambda < 1/(1 + |\sin(\phi_0)|)$ which is satisfied below the dashed white curve in Fig. 2. Our treatment thus applies to the first two bands for all incident angles, and in the the third band provided $|\phi_0| \lesssim 50^\circ$. We then see from Fig. 4, which shows the normal incidence transmittance of both a semi-infinite PC and its constituent grating, that their transmission maxima coincide almost perfectly.

To establish the link between the transmission of the grating and the PC, we return to the transfer matrix equation (1) and reduce this to a 2×2 matrix eigenvalue problem by dropping all but the propagating specular order. Proceeding formally, we are led to an eigenvalue equation which appears as a quadratic equation

$$\mu^2 - 2b\mu + 1 = 0, \quad \text{where} \quad b = \frac{T^2 - RR' + 1}{2T}, \quad (8)$$

where R and T refer to the specular order elements R_{00} and T_{00} of the respective grating scattering matrices. By reciprocity, $T = T'$, and for a square lattice geometry, up-down symmetry requires that $R = R'$. This allows b to be written in the simplified form $b = \cos(\arg |T|)/|T|$ —a consequence of the energy conservation properties $|R|^2 + |T|^2 = 1$ and $\arg(T) - \arg(R) = \pm\pi/2$. In a similar manner, we may derive a quadratic equation in $R_\infty = f_+/f_-$, that links directly the reflection characteristics of the semi-infinite PC and the transmission and reflection properties of the grating, namely,

$$R_\infty^2 - 2cR_\infty + 1 = 0, \quad \text{where} \quad c = -\frac{T^2 - R^2 - 1}{2R} = \frac{\cos(\arg |R|)}{|R|},$$

in which b and c are related by $c^2 - 1 = (1 - b^2)|T|^2/|R|^2$. Note that in a pass band, $|b| < 1$, and correspondingly, $c > 1$ or $c < -1$, yielding two real solutions for R_∞ that are reciprocals of one another, with the physical solution chosen according to $|R_\infty| < 1$. The low reflectance of the bulk PC then follows from the correspondingly low reflectance of the grating since

$$R_\infty \approx \frac{1}{2c} = \frac{|R|}{2 \cos(\arg |R|)}. \quad (9)$$

This is consistent with the results in Fig. 4, which clearly illustrates the coincidence of the near-zero reflectance features in the grating and the semi-infinite PC transmission spectra. Having now linked the properties of the bulk crystal to those of its gratings, we now turn to the final task of linking the properties of the grating to the resonant properties of its constituent cylinders.

4.2. Relationship between single-cylinder scattering and grating transmission properties

To establish a direct link between the cylinder scattering resonances and the concomitantly high transmittances of both the grating and the bulk PC, we need to consider the multipole formulation for diffraction of a plane wave by a grating composed of cylinders. The incident field is a plane wave δ which impinges from above at an angle ϕ_0 , giving rise to plane wave fields above and below the grating composed of a superposition of propagating and evanescent grating orders. As in Section 3, the field in the vicinity of each cylinder is expanded in terms of a cylindrical harmonic basis in the form of Eq. (4) where the b_n coefficients are again associated with the scattered field. This time, however, the a_n coefficients, which characterize the regular (non-singular) part of the field, are due to the outgoing field sourced on all other cylinders plus fields generated by exterior sources which, here, is the incident plane wave. We thus derive the matrix field identity¹²

$$a = Sb + J^- \chi^{-1/2} \delta \quad (10)$$

in which $S = [S_{lm}] = [S_{l-m}]$, with the S_n denoting the lattice sums

$$S_n = \sum_{s \neq 0} H_n^{(1)}(k|s|d) e^{-in \arg(s)} e^{i\alpha_0 s d} \quad (11)$$

that characterize the scattering contributions associated with a particular multipole order due to the entire grating. The matrix $J^- = [J_{np}^-]$, where $J_{np}^- = (-1)^n \exp(-in\phi_p)$ and $\exp(i\phi_p) = (\chi_p + i\alpha_p)/k$, performs a coordinate transformation from the plane wave basis to the cylindrical harmonic basis. Combining the single cylinder boundary conditions of Eq. (5) and the field identity in Eq. (10), we deduce the form of the outgoing scattered field

$$b = -(S' + iM)^{-1} J^- \chi^{-1/2} \delta \quad (12)$$

where $S' = S + I$ and I is the unit matrix. From this, the reflected and transmitted plane wave coefficients may be reconstructed¹²:

$$r = \frac{2}{d} \chi^{-1/2} K^+ b, \quad t = \delta + \frac{2}{d} \chi^{-1/2} K^- b, \quad (13)$$

where $K^+ = [K_{pn}^+]$, with $K_{np}^+ = \exp(-in\phi_p)$, and $K^- = [K_{pn}^-]$, with $K_{np}^- = (-1)^n \exp(in\phi_p)$. In the long wavelength case with only a single propagating order, these simplify, for normal incidence to,

$$r_0 = \frac{2}{d\chi_0^{1/2}} \sum_n b_n \quad (14)$$

$$t_0 = 1 + \frac{2}{d\chi_0^{1/2}} \sum_n (-1)^n b_n, \quad (15)$$

with $b_{-n} = b_n$, by symmetry. Thus, the respective amplitudes of the backward and forward scattered fields are proportional to $b_0 + 2b_1 + 2b_2 + \dots$ and $b_0 - 2b_1 + 2b_2 - \dots$, where the expression may be satisfactorily truncated to a given multipole order that depends on the frequency of the light.

We can now verify the empirical results of Section 3 that indicated a strong correlation between forward scattering by each cylinder and efficient transmission into the PC. To do so, we consider a modified form of the asymmetry parameter g (8) that allows us to directly compare results obtained through the grating and a single cylinder scattering theories. We need to do so because while in the case of a cylinder T_c is defined for all angles θ , the corresponding grating quantity is defined only for the directions of the grating spectral orders. We thus introduce a new asymmetry parameter for the single cylinder,

$$\tilde{g}_c = \frac{|T_c(-\pi/2)|^2 - |T_c(\pi/2)|^2}{|T_c(-\pi/2)|^2 + |T_c(\pi/2)|^2} = \frac{1 - \left| \frac{T_c(\pi/2)}{T_c(-\pi/2)} \right|^2}{1 + \left| \frac{T_c(\pi/2)}{T_c(-\pi/2)} \right|^2}. \quad (16)$$

which extends easily to a grating. Figure 5 compares the two parameters g and \tilde{g}_c and shows good qualitative agreement with respect to the forward scattering peaks and the shape of the curves. There are discrepancies between g and \tilde{g}_c when there is significant scattering into the backward half-plane ($0 < \theta < \pi$) but $T_c(\pi/2) \approx 0$ at the high-frequency end of Fig. 5. Nevertheless, the qualitative agreement between the curves is good at lower frequencies when the scattering is dominated by monopole and dipole terms. Accordingly, in the first and second bands, in which it was shown in Sec. 3 that a dipole approximation for $T_c(\theta)$ (6) is valid, we derive a simplified form for the ratio of the scattering amplitudes in Eq. (16)

$$\frac{T_c(\pi/2)}{T_c(-\pi/2)} = \frac{-1 + i(M_1 - 2M_0)}{3 + i(M_1 + 2M_0)}. \quad (17)$$

Since the M_n (5) are real, even when there is strong forward scattering, as in Fig. 3(g), a small, but finite, backscattered field remains, so that $\tilde{g}_c < 1$. However, we have observed from Fig. 4 that the transmission spectrum of the grating exhibits almost zero reflectance at approximately the same frequency.

To understand the difference that additional (phased) cylinders in the form of a grating can make, we must consider the grating equivalent of Eq. (16), namely

$$\tilde{g}_g = \frac{1 - \left| \frac{T_g(\pi/2)}{T_g(-\pi/2)} \right|^2}{1 + \left| \frac{T_g(\pi/2)}{T_g(-\pi/2)} \right|^2}, \quad (18)$$

where $T_g(-\pi/2) = r_0$ and $T_g(\pi/2) = t_0 - 1$ are the amplitudes of the scattered field components in the backward and forwards directions. Plotted on the same axes as g and \tilde{g}_c in Fig. 5 is \tilde{g}_g . Note that while the \tilde{g}_c and \tilde{g}_g curves have significantly different shapes, the locations of the forward scattering peaks are quite similar, with excellent agreement between all three curves close to the second peak at $d/\lambda \approx 0.6$. This demonstrates that forward scattering by each cylinder in a grating manifests itself as forward scattering by the grating, and hence to high transmission into the spectral grating order. What remains, however, is for us to demonstrate that a grating can effectively nullify, rather than just reduce, the reflectance.

To establish this connection we need to derive the grating equivalent of Eq. (17) which follows directly from a dipole order approximation for $T_g(\pi/2) = b_0 + 2b_1 = K^+ (S' + IM)^{-1} J^-$ and $T_g(-\pi/2) = b_0 - 2b_1 =$

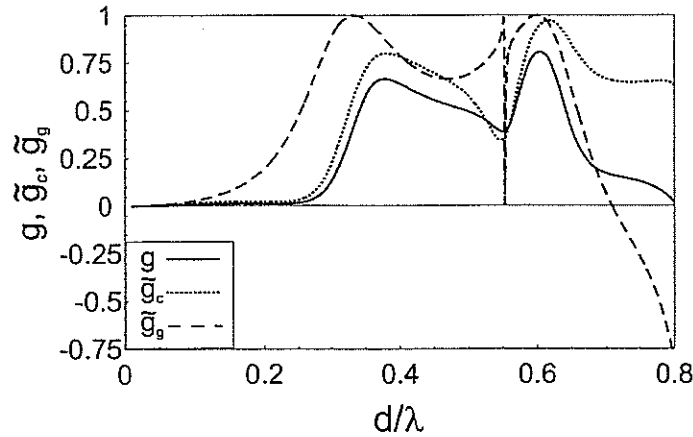


Figure 5. Comparison of single cylinder scattering parameters g (solid) and \bar{g}_c (dashed) for a cylinder of index $\nu_c = 3.0$ and radius $r_c = 0.34d$, and \bar{g}_g (dotted) for a grating of period d formed from identical cylinders. The horizontal axis is expressed in units of the normalised grating frequency, d/λ .

$K^- (S' + IM)^{-1} J^-$. This leads to

$$\frac{T_g(\pi/2)}{T_g(-\pi/2)} = \frac{(S'_2 - S'_0) + i(M_1 - 2M_0)}{(3S'_0 + S'_2) + i(M_1 + 2M_0)}, \quad (19)$$

which is similar in form to its cylinder analogue (17), particularly in the terms M_n involving the material properties. However, there are subtle, but important, differences in the form of the lattice sums S'_m introduced by the addition of an array of periodically phased cylinders.

The lattice sums have explicit forms that have been derived by Twersky¹⁵ and by Nicorovici *et al.*,¹⁶:

$$S'_{2l} = S'^J_{2l} + iS'^Y_{2l}, \quad S'_{2l-1} = iS'^J_{2l-1} - S'^Y_{2l-1} \quad (20)$$

where

$$S'^J_{2l} = \frac{2}{d} \sum_{p \in \Omega_p} \frac{\cos(2l\phi_p)}{\chi_p}, \quad S'^J_{2l-1} = \frac{2}{d} \sum_{p \in \Omega_p} \frac{\sin((2l-1)\phi_p)}{\chi_p} \quad (21)$$

with Ω_p denoting the set of propagating plane wave orders with propagation angles ϕ_p and where the quantities S'^J_{2l} and S'^Y_{2l} are real. For normal incidence and a single propagating order, $S'^J_0 = S'^J_2 = 2/(\chi_0 d) = 2/(kd)$, thus further simplifying Eq. (19) to

$$\frac{T_g(\pi/2)}{T_g(-\pi/2)} = \frac{i(S'^Y_2 - S'^Y_0 + M_1 - 2M_0)}{(3S'_0 + S'_2) + i(M_1 + 2M_0)}. \quad (22)$$

What distinguishes Eq. (22) from Eq. (17) is that the numerator of the former is purely imaginary, rather than being complex. This simple transformation introduces the possibility of a null reflectance since a zero of $r_0 \propto T_g(\pi/2)$, corresponding to $\bar{g}_g = 1$, can be more easily realized through the solution of a single equation, than through the solution of two simultaneous equations. It is clear from Fig. 6(a) that such a zero can be realized and that it exactly predicts the location of the null reflectance of the grating, and in turn of the semi-infinite crystal.

The procedure can be generalized to the case of off-normal incidence, provided that only a single order is propagating and we adjust the formulation so that for an incident angle of ϕ_0 , the backward scattering amplitude is defined as $T_g(\pi/2 - \phi_0)$ and the forward scattering amplitude is $T_g(-(\pi/2 - \phi_0))$. This procedure can also be generalized to quadrupole accuracy and beyond. However, we do not discuss this here as the analysis is substantially more complicated. Nevertheless, to the same dipole order accuracy, one can show that the numerator of $T_g(\pi/2 - \phi_0)/T_g(-(\pi/2 - \phi_0))$ can again be rendered either purely real or purely imaginary, thus admitting the possibility of a genuine null reflectance. This is illustrated in Fig. 6(b)–(h) for a wide range of

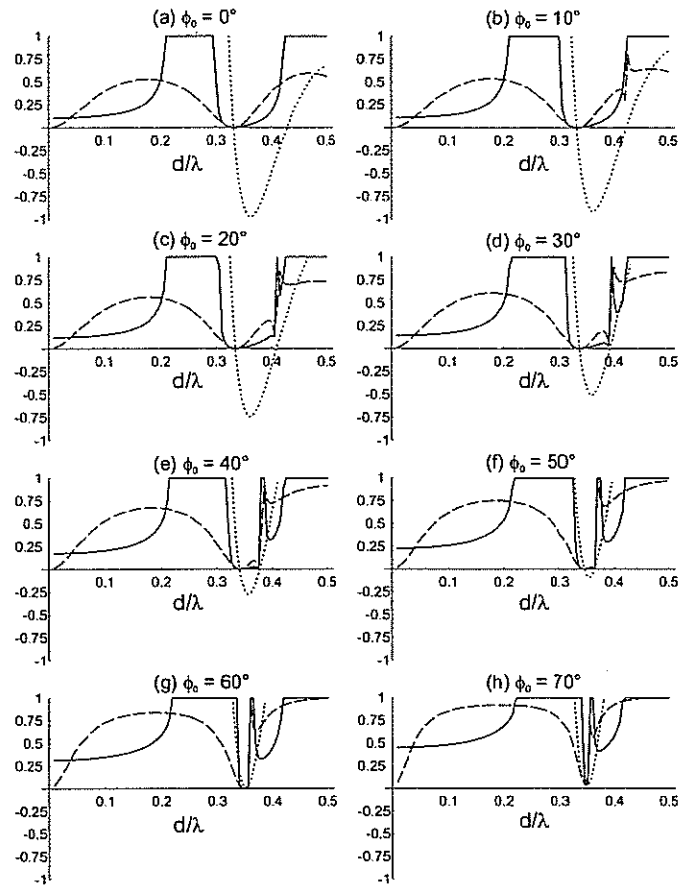


Figure 6. Plots of the numerator of the back scattering amplitude, $T_g(\pi/2 - \phi_0)$ (dotted), the reflectance of a single grating (dashed) and the semi-infinite PC (solid) as a function of normalised frequency d/λ for $\phi_0 = 0^\circ - 70^\circ$ in 10° increments. Calculations are to dipole order accuracy.

angles of incidence, from which it is apparent that the reflection null is remarkably insensitive to the incidence direction. This insensitivity to the angle of incidence can be understood by considering the five key quantities involved in the dipole order approximation—three lattice sums S'_0 , S'_1 and S'_2 , all of which are only slow functions of the angle of incidence and frequency, and the boundary condition terms M_0 and M_1 . Figure 3(d) shows that b_1 passes through a resonance close to the reflection null, and hence it is clear that M_1 is the critical term, with its rapid change dominating the calculation and rendering the location of the reflection null largely insensitive to the angle of incidence, and close to the single cylinder resonance.

For shorter wavelengths, however, for which there can be more than one propagating order, $T_g(\pi/2)$ cannot be simplified so that it has a real numerator, even for the simplest, most highly symmetric cases. The need to solve two independent simultaneous equations to locate a zero of $T_g(\pi/2)$ is much more complicated and from our computational studies, we believe that there is no zero that can be deduced for real incidence parameters. Accordingly, the near-perfect transmission into a photonic crystal thus appears limited to the case of long wavelengths (i.e., single propagating orders in reflection and transmission). As we discuss in the next section, this result has significant implications for coupling to hole-type PCs.

5. APPLICABILITY OF THE RESULTS FOR 3D SLABS

We now extend the results derived in 2D, showing that they are generic and applicable to a 3D PC slab geometry.¹⁷ Figure 7 illustrates the geometry that we consider, where appropriate boundary conditions are used to simulate a semi-infinite cladding extending above and below the core slab, and in the xz -plane. This geometry

is similar to that proposed by Martinez *et al.*¹⁸ with cylinder radius $r_c = 0.35d$ and slab height $h = 3d$. Three-dimensional finite difference time domain (FDTD) results are presented in addition to 2D Bloch mode matrix method (BMM) calculations⁴ outlined earlier. In the FDTD simulations, an elliptical Gaussian beam with full widths at half maximum (FWHM) of $w_{xz} = 5d$ and $w_y = 2.5d$ is launched with *TM* polarization (electric field along the *y*-axis) at an incident angle ϕ_0 relative to the normal of the PC interface. The crystal is oriented such that the normal is parallel to the Γ -*M* axis of the hexagonal Brillouin zone. The 2D calculations, with rods of index $\nu_c = 3.4$ in a background of index $\nu_b = 1.458$, are a good approximation to the 3D simulations, thus providing an efficient tool for optimizing parameters before launching computationally intensive 3D simulations.

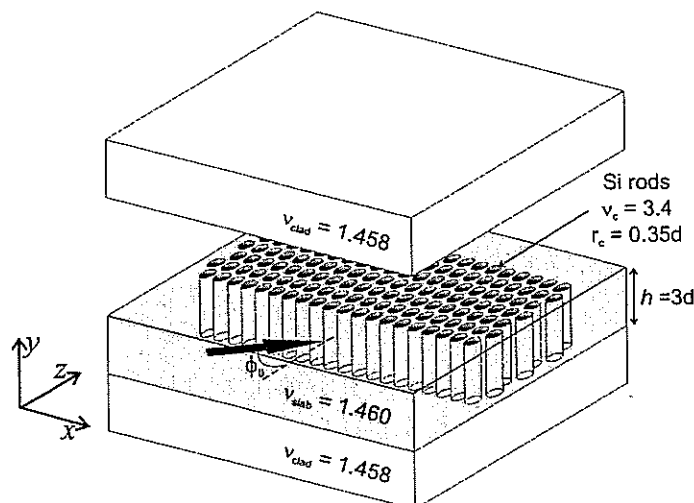


Figure 7. Geometry of the PC slab with core and cladding index $\nu_{\text{slab}} = 1.460$ and $\nu_{\text{clad}} = 1.458$. The upper cladding is lifted to show the interior structure. The triangular PC lattice is formed by cylinders of height $h = 3d$, index $\nu_c = 3.4$ and radius $r_c = 0.35d$, where d is the lattice period.

Figure 8 shows the reflectance spectra for Gaussian beams with $\phi_0 = 0^\circ$ (solid curve) and $\phi_0 = 22.5^\circ$ (long dashed curve) incident on 16 layers of the PC in Fig. 7. These results were calculated with the 3D FDTD software FullWAVE with perfectly matched layer boundary conditions on all sides of the computational domain. Also shown are the equivalent reflectance ($|R_\infty|^2$) spectra for plane waves incident on a 2D semi-infinite PC, calculated using the Bloch mode matrix method.⁴ On all curves, the minimum reflected power occurs for scaled frequencies $0.29 < d/\lambda < 0.295$, with bandwidths of more than 15% of the central frequency where the reflectance is below 10%. The 3D simulations show a minimum reflectance of 0.2% and 1.4% for $\phi_0 = 0^\circ$ and $\phi_0 = 22.5^\circ$ respectively, compared to less than 0.1% in the 2D results, a variation attributed to the angular spread of the Gaussian beam in the 3D calculations. The Fabry-Perot fringes in the FDTD results are weak at oblique incidence because of finite beam effects.

Such efficient coupling over a wide range of angles is far superior to the published results for air hole PCs and is a generic feature of high index PCs that occurs under two conditions. Firstly, as deduced in our 2D analysis, most of the incident light must be forward scattered by each cylinder. Secondly, when each layer of cylinders is considered as a grating, only a single propagating grating order exists. The first condition is not satisfied in the first band or for low index contrasts, since in these cases light is scattered almost isotropically by the cylinders.¹¹ If the frequency $d/\lambda > 1/\nu_b$, (in the case of normal incidence) multiple diffracted orders appear, with interference between orders reducing the efficiency. There is thus a limited frequency range in which almost perfect coupling can occur. We have found that in most realistic 2D rod-type PCs, the second and sometimes the third band can exhibit this property in both triangular and square lattices, and for *TE* and *TM* polarization.

6. DISCUSSION AND CONCLUSIONS

Since efficient coupling relies on the properties of the individual inclusions, it occurs for a wide range of rod-type photonic crystals. We analyzed the case of *TM* polarized light here in detail, and have observed similarly

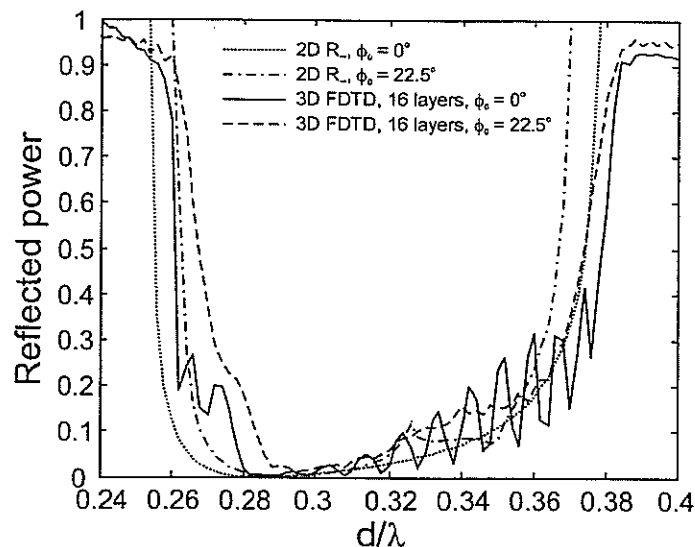


Figure 8. 2D plane wave reflectance spectra (Bloch mode matrix method) for a semi-infinite PC and 3D FDTD reflectance spectra for a Gaussian beam of width $w_{xz} = 5d$ and $w_y = 2.5d$ incident on 16 layers of cylinders. Results are shown for $\phi_0 = 0^\circ$ and $\phi_0 = 22.5^\circ$.

efficient coupling for TE polarization, although we have not analyzed this case to the same extent. It would be interesting to study whether similar effects occur for air hole PCs. As a first comment, note that in such PCs, it is much more difficult to satisfy the simultaneous conditions of the occurrence of a single grating order and a forward scattering resonance of the inclusions. This is so because non-isotropic scattering from air holes only occurs at relatively high frequencies but at the same time the high index background material reduces the frequency at which multiple plane wave orders appear. We analyzed air-hole type PCs with polarized light for a range of refractive index contrasts, and found that the two conditions are never simultaneously satisfied. For TE polarization we analyzed a air-hole type PC with index contrast of 3 and did not find a wavelength where efficient coupling occurs. However, we have not considered lower index contrasts for this polarization yet.

In conclusion, efficient coupling into rod-type has been demonstrated theoretically and numerically. The effect is associated with the scattering resonance of the individual conclusions. We linked these properties to those of the full PC via the properties of the gratings that make up the PC. Though the effect is clearest in 2D systems, it carries over to fully 3D systems as well.

7. ACKNOWLEDGEMENTS

This work was produced with the assistance of the Australian Research Council under the ARC Centres of Excellence program.

REFERENCES

1. T. Baba and D. Ohsaki, "Interfaces of photonic crystals for high efficiency light transmission," *Japan. J. Appl. Phys.* **40**, pp. 5920-5924, 2001.
2. B. Momeni and A. Adibi, "Adiabatic matching stage for coupling of light to extended bloch modes of photonic crystals," *Appl. Phys. Lett.* **87**, p. 171104, 2005.
3. J. Witzens and A. Scherer, "Efficient excitation of self-collimated beams and single bloch modes in planar photonic crystals," *J. Opt. Soc. Am. A* **20**, pp. 935-940, 2003.
4. L. C. Botten, T. P. White, A. A. Asatryan, T. N. Langtry, C. M. de Sterke, and R. C. McPhedran, "Bloch mode scattering matrix methods for modeling extended photonic crystal structures. part i: Theory," *Phys. Rev. E* **70**, p. 056606, 2004.

5. T. P. White, L. C. Botten, C. M. de Sterke, R. C. McPhedran, A. A. Asatryan, and T. N. Langtry, "Bloch mode scattering matrix methods for modeling extended photonic crystal structures. part ii: Applications," *Phys. Rev. E* **70**, p. 056607, 2004.
6. D. Maystre, "Integral Methods, in *Electromagnetic Theory of Gratings*, Topics in Current Physics vol. 22, Ed. R. Petit, pp. 63100, Springer Verlag, Berlin, 1980.
7. M. Nevière and E. Popov, *Light propagation in periodic media*, Marcel Dekker, New York, 2003.
8. L. C. Botten et al, "From multipole methods to photonic crystal device modelling, in *Electromagnetic theory and applications for photonic crystals*, K. Yasumoto, ed., pp. 47122, CRC Taylor and Francis, Boca Raton, 2006.
9. E. N. Economou and A. Zdetsis, "Classical wave propagation in periodic structures," *Phys. Rev. B* **40**, pp. 1334-1337, 1989.
10. C. M. Soukoulis, ed., *Photonic bandgaps and localization*, Plenum Press, New York, 1993.
11. H. C. van de Hulst, *Light scattering by small particles*, John Wiley and Sons, New York, 1957.
12. L. C. Botten, N. A. Nicorovici, A. A. Asatryan, R. C. McPhedran, C. M. de Sterke, and P. A. Robinson, "Formulation for electromagnetic scattering and propagation through grating stacks of metallic and dielectric cylinders for photonic crystal calculations. part 1: Method," *J. Opt. Soc. Am. A* **17**, pp. 2165-2176, 2000.
13. M. Abramowitz and I. A. Stegun, eds., *Handbook of Mathematical Functions*, Dover Publications, New York, 9 ed., 1970.
14. E. Lidorikis, M. M. Sigalas, E. N. Economou, and C. M. Soukoulis, "Tight-binding parametrization for photonic band gap materials," *Phys. Rev. Lett.* **81**, pp. 1405-1408, 1998.
15. V. Twersky, "Elementary function representations of schlömilch series," *Arch. Ration. mech. Anal.* **8**, pp. 323-332, 1961.
16. N. A. Nicorovici and R. C. McPhedran, "Lattice sums for off-axis electromagnetic scattering by gratings," *Phys. Rev. E* **50**, pp. 3143-3160, 1994.
17. T. P. White, C. M. de Sterke, R. C. McPhedran, and L. C. Botten, "Highly efficient wide-angle coupling into uniform rod-type photonic crystals," *Appl. Phys. Lett.* **87**, p. 111107, 2005.
18. A. Martinez, J. Garcia, G. Sanchez, and J. Marti, "Planar photonic crystal structure with inherently single-mode waveguides," *J. Opt. Soc. Am. A* **20**, pp. 2131-2136, 2003.